Metals and Materials International (2021) 27:2205–2219
https://doi.org/10.1007/s12540-020-00609-9

A Review on Silicide-Based Materials: Thermoelectric and Mechanical Properties

Gwansik Kim[1] · Hyunjun Shin[1] · Jihyun Lee[1] · Wooyoung Lee[1]

Received: 1 October 2019 / Accepted: 3 January 2020 / Published online: 24 January 2020

Abstract
Silicide-based thermoelectric (TE) materials are promising candidates for automotive TE generators, which can collect wasted heat and convert it into electricity. Adequate strategies should be used to manufacture highly efficient silicide-based TE devices. This review summarizes novel strategies for obtaining materials that feature excellent TE properties and mechanical reliability. Controlling the carrier concentration and band structure could increase their electronic transport properties, while nanostructure engineering could effectively reduce their lattice thermal conductivity. Moreover, well designed microstructures are required to obtain mechanically reliable TE materials, which indicates that precisely controlling their nanostructure is essential for the improved trade-off relationship between TE and mechanical properties. While many challenges should still be overcome, the development of highly efficient TE materials and devices could represent new solutions for the global energy crisis.

Keywords Thermoelectric materials · Silicide · Mg_2Si · Higher manganese silicide

1 Introduction

1.1 Thermoelectricity

Renewable energy is a research area that is gaining global attention owing to environmental pollution concerns and the exhaustion of fossil fuel resources. Particularly, air pollution from fossil fuel used for fueling vehicles and in industries is a concerning global problem. The thermoelectric (TE) technology involves the direct and reversible conversion between thermal energy and electrical energy that is generated as electrons or holes move owing to temperature differences. Given that more than 60% of energy is wasted as heat during the energy generation and consumption process, thermoelectric power generation (TEG) is a promising energy generating technology. TEG devices present great advantages, including long life and high degree of environmental friendliness. Moreover, they can be manufactured in various areas from local to large areas. However, TEG devices are still difficult to commercialize owing to their low energy efficiency and mechanical reliability, and also their price competitiveness. The efficiency of TEG devices can be calculated as follows:

$$\eta = \frac{T_h - T_c}{T_h} \cdot \frac{\sqrt{1+Z\overline{T}}-1}{\sqrt{1+Z\overline{T}}+\frac{T_c}{T_h}}, \tag{1}$$

where T_h and T_c are the temperatures of the hot and cold sides, respectively, $\overline{T}$ is the average of T_h and T_c, and ZT is a dimensionless figure of merit. This dimensionless figure of merit can be used to evaluate TE materials and has been defined as:

$$ZT = \sigma S^2/\kappa \tag{2}$$

where σ, S, T, and κ are the electrical conductivity, Seebeck coefficient, absolute temperature, and total thermal conductivity of the material, respectively. TEG devices consist of a TE material, electrodes, paste materials, and diffusion barriers. Among these, the TE material is the most important component that determines their efficiency. Therefore, various strategies should be established to allow researchers to obtain materials with high ZT and excellent mechanical reliability and to develop inexpensive manufacturing processes [1].

✉ Wooyoung Lee
wooyoung@yonsei.ac.kr

[1] Department of Materials Science and Engineering, Yonsei University, Seoul 03722, Republic of Korea

1.2 Silicide-Based TE Materials

Recently, various TE materials featuring high *ZT* values have been researched, including skutterudites, half-Heusler alloys, silicides, and chalcogenides (Fig. 1 and Table 1) [2–23]. The *ZT* value of $Bi_{0.52}Sb_{1.48}Te_3$, which presented dense dislocations, was ~ 2.0 at low temperature [2], while those of PbTe-, Ag–Pb–Sb–Te-, and SnSe-based TE materials were as high as ~ 2.5 at mid-to-high temperature [14, 16, 21, 22]. However, most TE materials that present very high *ZT* values contain expensive and toxic elements, and therefore, can be difficult to commercialize. Because Bi and Te are very rare, they are also very expensive. Moreover, the use of Pb and Se has been gradually reduced worldwide owing to their toxicity. Therefore, cost and toxicity considerations are essential when developing TE materials. Consequently, silicide-based materials could be promising candidates for TE materials and devices. Silicide-based TE materials have received significant attention as automotive thermoelectric generators (ATEGs) owing to their low density, low cost, and non-toxicity.

Magnesium silicide (Mg_2Si) and higher manganese silicide (HMS) are representative *n*- and *p*-type silicide-based TE materials, respectively. Mg_2Si presents cubic structure (Fm3m space group) and a narrow bandgap (~ 0.77 eV) [4]. Generally, the *ZT* of un-doped Mg_2Si is lower than 0.1 owing to its very low electrical conductivity. However, the *ZT* of doped Mg_2Si could reach 1.0 at 873 K [4]. Moreover, the maximum *ZT* of ~ 1.5 was attributed to its high *S* and low κ values in Mg_2(Si, Sn) solid solution [24]. Additionally, controlling the Mg/Si ratio and the secondary phases, such as Si and MgO are effective route for enhancing the TE properties and ensure the thermal and chemical stability of Mg_2Si [25, 26]. Despite its high *ZT* values, the applications of Mg_2Si have been limited owing to its low mechanical reliability (fracture toughness, K_{Ic}, value of ~ 0.82 MPa $m^{1/2}$), which suggested that more research into the mechanical reliability of TE materials is required to fabricate efficient TEG devices [27].

Unlike Mg_2Si, HMS exhibits complex tetragonal crystal structure (Mn sub-lattices (chimneys) and interpenetrating helical Si sub-lattices (ladders)) known as the Nowotny Chimney Ladder (NCL) structure [28]. Moreover, depending on their Mn-to-Si atomic ratio, HMS presents different phases, including Mn_4Si_7, $Mn_{11}Si_{19}$, $Mn_{15}Si_{26}$, and $Mn_{27}Si_{47}$, which are NCL phases of various stoichiometry [28]. Although HMS phases exhibited the different lattice parameters ($a = b = 5.52$–5.53 Å and c = 17.46–117.90 Å) and space groups (P$\bar{4}$c2, P$\bar{4}$ n2, I$\bar{4}$2d, and P $\bar{4}$n2), their electronic band structure (0.76–0.78 eV) and intrinsic TE properties (*ZT* = ~ 0.4 at 700–800 K) are similar [29–32]. The MnSi and Si secondary phases of HMS negatively affect their TE properties. Therefore, suppressing the secondary phases generation is essential for achieving good TE properties by optimizing the fabrication process and performing compositional tuning [33–35]. The *ZT* values of HMS doped at the Mn- and Si-sites have been reported to be as high as 0.6. Furthermore, nanocomposite engineering strategies have been used to improve the TE properties of doped HMS by manipulating their electronic and thermal transport properties [8]. Despite their low *ZT* values compared with those of Mg_2Si, HMS exhibits excellent mechanical, chemical, and thermal stability, and therefore, novel strategies for improving their TE properties are required.

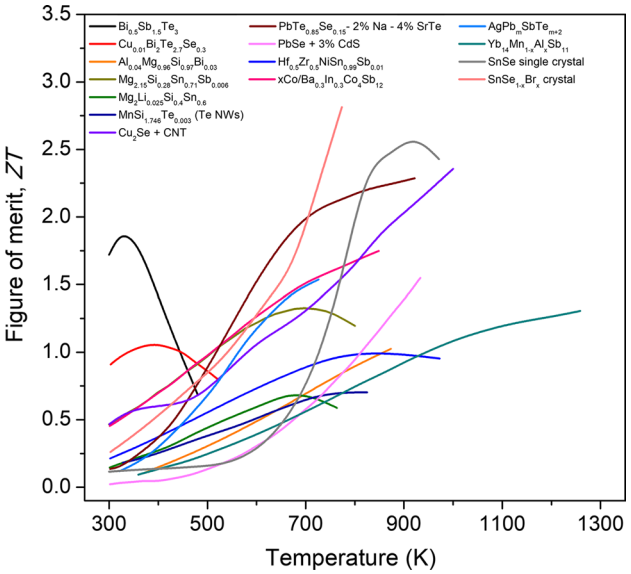

Fig. 1 Figure of merit, *ZT*, as function of temperature for typical thermoelectric materials. Here, *NWs* nanowires and *CNT* carbon nanotube

Herein, we summarize the strategies for improving the TE properties and mechanical reliability of silicide-based TE materials. We also demonstrate the importance of microstructure and band structure control to obtain the high TE properties and mechanical reliability of silicide-based TE materials. Lastly, we suggest development directions and provide material design guidelines for silicide-based TE materials to obtain highly efficient TEG devices.

2 Increasing *ZT* of Silicide Bulk Materials

2.1 Compositional Tuning and Optimizing n_c

The individual relationships between *S*, σ, and κ and n_c, can be expressed using the following equations:

$$S = \frac{8\pi^2 k_B^2}{3eh^2} m^* T \left(\frac{\pi}{3n_c}\right)^{2/3}, \quad (3)$$

Table 1 Thermoelectric properties of state-of-art thermoelectric materials

Material	Carrier type	*PF* (μW cm^{-1} K^{-2})	κ_{tot} (W m^{-1} K^{-1})	κ_{lat} (W m^{-1} K^{-1})	*T* (K)	*ZT*	Synthetic method[a]	References
$Bi_{0.5}Sb_{1.5}Te_3$	*p*	37.79	0.65	0.34	320	1.86	MS-SPS	[2]
$Cu_{0.01}Bi_2Te_{2.7}Se_{0.3}$	*n*	29.71	1.12		398	1.06	BM-HP	[3]
$Al_{0.04}Mg_{0.96}Si_{0.97}Bi_{0.03}$	*n*	28.8	2.45	0.88	873	1.02	SSR-SPS	[4]
$Mg_{2.15}Si_{0.28}Sn_{0.71}Sb_{0.006}$	*n*	44.32	2.33		700	1.30	SSR-SPS	[5]
Sb doped $Mg_2Si_{0.5}Sn_{0.5}$	*n*	25.81	0.98	0.49	615	1.63	Melting-SPS (press-less sintering)	[6]
$Mg_2Li_{0.025}Si_{0.4}Sn_{0.6}$	*p*	14.31	1.30		675	0.70	Melting-PECS	[7]
$MnSi_{1.746}Te_{0.003}$ (Te NWs)	*p*	15.88	1.87	1.47	823	0.70	Wet BM-SPS	[8]
$Re_{6.0}Mn_{30.4}Si_{63.6}$	*p*	23.10	2.09	1.01	920	1.04	SSR-BM-SPS	[9]
$Hf_{0.5}Zr_{0.5}NiSn_{0.99}Sb_{0.01}$	*n*	49.27	4.47	2.04	873	1.00	AM-BM-HP	[10]
$xCo/Ba_{0.3}In_{0.3}Co_4Sb_{12}$	*n*	51.98	2.53	0.71	850	1.75	Melting-SPS	[11]
$(Sr, Ba, Yb)_yCo_4Sb_{12}$	*n*	44.42	2.06		835	1.80	SSR-HP	[12]
PbTe/PbSe nanoparticles	*n*	26.61	0.87	0.40	623	1.85	Solution based reaction + SPS	[13]
$PbTe_{0.85}Se_{0.15}$–2% Na–4% SrTe	*p*	23.50	0.96	0.46	923	2.30	Melting-SPS	[14]
PbTe–SrTe doped with Na_2Te (2 mol%)	*p*	19.28	0.94	0.46	800	1.70	Melting	[15]
PbTe–SrTe doped with 2 mol% Na	*p*	23.88	0.97	0.53	915	2.20	Melting-SPS	[16]
PbSe + 3% CdS	*p*	16.96	0.99	0.64	923	1.60	Melting-SPS	[17]
Cu_2Se + CNT	*p*	8.79	0.37		1000	2.40	BM-SPS	[18]
$Yb_{14}Mn_{1-x}Al_xSb_{11}$	*p*	5.55	0.52		1223	1.30	Flux method	[19]
$AgPb_mSbTe_{m+2}$	*n*	15.35	0.72		723	1.54	BM-SPS	[20]
$SnSe_{1-x}Br_x$ crystal	*n*	8.98	0.25	0.20	773	2.80	Bridgman method	[21]
SnSe single crystal	*p*	9.90	0.35		923	2.60	Bridgman method	[22]

[a]*MS* melt spinning, *SPS* spark plasma sintering, *BM* ball milling, *HP* hot pressing, *SSR* solid state reaction, *IM* induction melting, *PECS* pulsed electric current sintering, and *AM* arc melting

$$\sigma = n_c e \mu_{Hall}, \tag{4}$$

and

$$\kappa = L\sigma T = Ln_c e \mu_{Hall} T, \tag{5}$$

where m^*, ρ, and μ_{Hall} are the effective mass, electric resistivity, and Hall mobility, respectively, e is the electron charge, k_B is the Boltzmann constant, and L is the Lorenz number. These relationships indicate that control of n_c is a key strategy for achieving high *ZT* values. The optimization of n_c via doping is essential for improving the TE properties of silicide-based TE materials, owing to their low *ZT* values (~0.1 and ~0.4 for Mg_2Si and HMS, respectively) [33, 36]. Sb and Bi are the main *n*-type doping elements that replace the Si sites, and Al is another *n*-type doping element that substitutes the Mg sites of Mg_2Si-based compounds [4, 36–40]. Various other dopants, such as Y, Te, and Pb were also used, however, the increase in the TE properties of the Mg_2Si-based materials was insufficient (Fig. 2 and Table 2) [41–44]. Sb and Bi doping caused n_c to increase, which led to the increase in σ and decrease in the lattice thermal conductivity (κ_{lat}) via point defect phonon scattering [36–38]. Kim et al. were able to obtain a Mg_2Si-based material featuring the *ZT* value of 1.0 at 873 K by optimizing its n_c (0.9×10^{20}–1.2×10^{20} cm^{-3}) and controlling the solubility of Bi via a co-doping strategy [4].

Using doping element control, it is possible to obtain Mg_2Si-based compounds that feature *p*-type characteristics. Li, Na, and Ga are representative *p*-type doping elements. Among them, Li and Na are substitutional dopants at the Mg site, and Ga is a dopant at the Si site (Fig. 3 and Table 3) [7, 45–52]. The *p*-type Mg_2Si comprises doped Mg_2Si–Mg_2Sn and Mg_2Sn-Mg_2Ge solid solutions. The presence of these solid solutions increased the *S* value of the *p*-type Mg_2Si owing to band convergence and decreased its κ_{lat} value owing to intensified phonon scattering [7, 45–49]. The *ZT* value of the *p*-type Mg_2Si was 0.7 at 675 K, which was still lower than that of the *n*-type Mg_2Si [7].

Typically, HMS is generally known to be the *p*-type counterparts of Mg_2Si-based TE materials. The TE properties of the undoped HMS are poor (*ZT* ~ 0.4) [33] and their n_c are relatively high (1.1×10^{21}–2.7×10^{21} cm^{-3}) [53]. V, Cr, Fe, Co, W, and Re were investigated as doping elements at the Mn sites, and Al and Ge were studied as doping elements

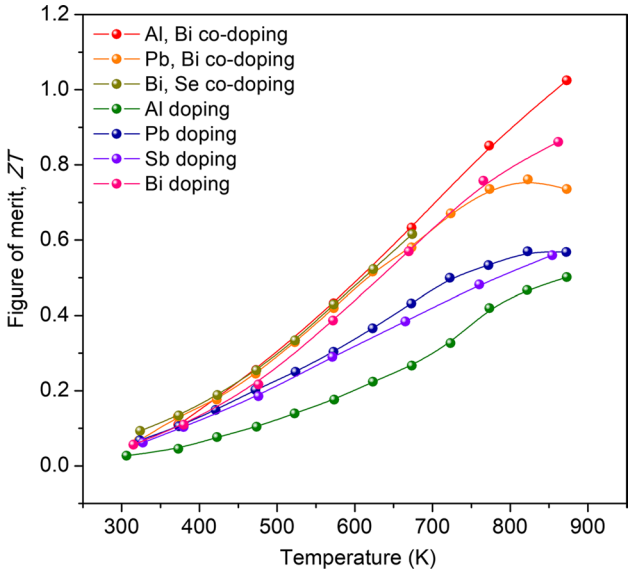

Fig. 2 Figure of merit, *ZT*, as function of temperature for *n*-type doped Mg_2Si

at the Si sites of HMS (Table 4) [9, 35, 54–67]. Chen et al. obtained HMS that presented the *ZT* value of 0.57 at 800 K via intensified phonon scattering. This high *ZT* value was attributed to the presence of point defects and the formation of $ReSi_{1.75}$ nanoinclusions, which were induced by Re doping [35]. She et al. reported Ge-doped HMS that presented the *ZT* value of 0.62 at 840 K by optimizing n_c, increasing m^*, and reducing κ_{lat} [64]. However, because n_c optimization strategies are limited owing to the doping solubility limit, novel processes such as gas atomization, rapid solidification, and shock wave were used to improve the TE properties of doped HMS by rapidly decreasing κ_{lat} [9, 55, 57, 66, 67]. Ge and Re co-doping combined with the shock wave process generated high density dislocations, which resulted in the high *ZT* value (~ 1.0) of the co-doped HMS (Fig. 4) [67].

Controlling the n_c of Mg_2Si and HMS by controlling their Mg and Si contents, respectively, has been studied. However, the increase in their TE properties obtained by controlling n_c was insufficient. Therefore, manipulating the electronic and thermal transport properties of Mg_2Si and HMS by controlling their band structure and nanostructure should be considered to achieve materials with significantly improved TE properties.

2.2 Nanostructure Engineering

Nanostructure engineering is a conventional strategy for improving TE properties by decreasing κ_{lat}. Nanograins, heterostructures, nanophases, and nanoinclusions are effective for reducing κ_{lat} by controlling the interface properties of materials (Fig. 5a–c) [1, 68]. According to calculation

Table 2 Thermoelectric properties and typical synthesis methods of *n*-type doped Mg_2Si

Material	Dopant	n_c (10^{20} cm^{-3})	σ (S cm^{-1})	S (μV K^{-1})	PF (μW cm^{-1} K^{-2})	κ_{tot} (W m^{-1} K^{-1})	κ_{lat} (W m^{-1} K^{-1})	T (K)	ZT	Synthesis method[a]	References
$Al_{0.04}Mg_{0.96}Si_{0.97}Bi_{0.03}$	Al, Bi	1.14	766.87	− 193.86	28.80	2.45	0.88	873	1.02	SSR-SPS	[4]
$Mg_2Si_{0.98}Pb_{0.01}Sb_{0.01}$	Sb, Pb		719.99	− 202.21	29.44	3.19	1.86	823	0.76	BM-SPS	[41]
$Mg_2Si_{0.98}Pb_{0.01}Bi_{0.01}$	Pb, Bi		527.56	− 224.63	26.62	3.14	2.00	873	0.74	BM-SPS	[41]
$Mg_2Si_{0.98}Sb_{0.01}Bi_{0.01}$	Sb, Bi		580.62	− 205.75	24.58	2.82	1.59	873	0.76	BM-SPS	[41]
$Mg_{2.1}Si_{0.96}Bi_{0.02}Se_{0.02}$	Se, Bi	0.96	925.926	− 183.33	31.12	3.43		673	0.61	IM-induction assisted hot uniaxial press	[42]
Al0.01-doped Mg_2Si	Al		309.69	− 248.15	19.07	3.33		873	0.50	BM-SPS	[39]
Mg_2Si:Sb = 1:0.02	Sb	1.50	585.75	− 203.45	24.25	3.73		862	0.56	SPS	[37]
Mg_2Si + Bi 0.15 at.%	Bi	0.78	540.54	232.80	29.74	3.07	2.42	775	0.74	BM-HP	[38]
Mg_2Si:Bi = 1:0.02	Bi	1.10	548.88	− 252.66	35.04	3.51		862	0.86	SPS	[36]
2 at.% Pb doped Mg_2Si	Pb		175.47	− 285.98	14.35	2.11		823	0.56	BM-SPS	[43]
Mg_2Si + 2000 ppm Y	Y		175.00	− 311.70	17.00	4.30		600	0.23	BM-FAPAS	[44]

[a]*IM* induction melting, *FAPAS* field activated and pressure assisted synthesis

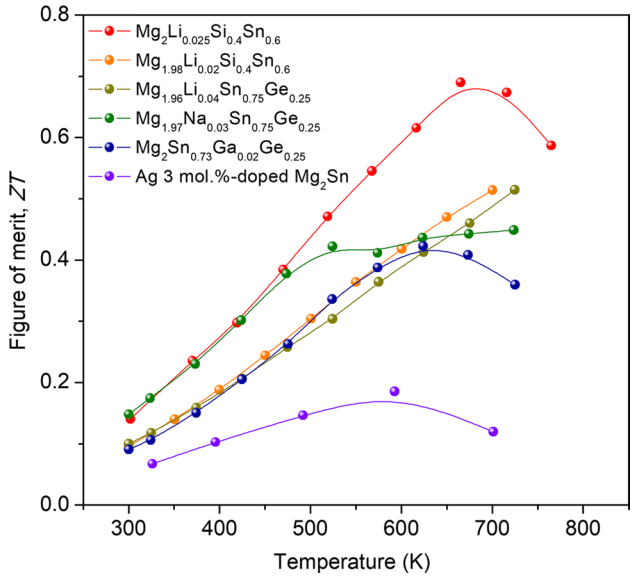

Fig. 3 Figure of merit, *ZT*, as function of temperature for *p*-type doped Mg_2Si

results previously reported, the increase in interface density is accompanied by the decrease in κ_{lat} and μ_{Hall} because for silicide-based TE materials the mean free paths of phonons and electrons are similar [69–71]. Therefore, nanocomposite engineering strategies, such as the introduction of nanophases and heterostructures, are more effective for manipulating the electronic and thermal transport properties of silicide-based TE materials.

SiC, multi-wall carbon nanotube (MWCNT), reduced graphene oxides (rGOs), metal nanoparticles (NPs), and Si were added to Mg_2Si to increase its TE properties (Fig. 6 and Table 5) [27, 34, 68, 72–79]. However, the *ZT* values of all nanocomposites were lower than those of pristine samples. Kim et al. investigated the relationship between the TE and mechanical properties by introducing various nanophases, such as metal NPs, rGOs, and also via dual nanoinclusion. They reported that the TE properties of all nanocomposites decreased owing to the significant decrease in their μ_{Hall} values, despite the decrease in thermal conductivity [27, 68, 77, 78]. Moreover, Yin et al. confirmed the decrease in the TE properties of $Mg_{2.16}(Si_{0.3}Sn_{0.7})_{0.98}Sb_{0.02}$/SiC nanowire or $Mg_{2.16}(Si_{0.3}Sn_{0.7})_{0.98}Sb_{0.02}$/SiC nanoparticles nanocomposites [72]. The power factors of Mg_2Si nanocomposites were low owing to their unfavorable band alignment induced by the low work function of Mg_2Si (3.59 eV) [80]. The decrease in κ_{lat} caused by the introduction of nanophases was insufficient because the main scattering centers of Mg_2Si-based TE materials were point defects.

Conversely, HMS nanocomposites have been relatively effective in improving TE properties (Fig. 7 and Table 6) [8, 34, 81–85]. The *ZT* values of HMS nanocomposites with Te

Table 3 Thermoelectric properties and typical synthesis methods of the *p*-type doped Mg_2Si

Material	Dopant	n_c (10^{20} cm^{-3})	σ (S cm^{-1})	S (μV K^{V1})	PF (μW cm^{-1} K^{-2})	κ_{tot} (W m^{-1} K^{-1})	κ_{lat} (W m^{-1} K^{-1})	T (K)	ZT	Synthesis method[a]	References
$Mg_{1.98}Li_{0.02}Si_{0.4}Sn_{0.6}$	Li	0.86	304.42	204.24	12.90	1.55		650	0.54	BM-SPS	[45]
$Mg_2Li_{0.025}Si_{0.4}Sn_{0.6}$	Li	0.80	303.66	216.68	14.26	1.30		675	0.70	SSR-PECS	[7]
$Mg_{1.86}Li_{0.14}Si_{0.4}Sn_{0.6}$	Li	2.70	488.37	178.13	15.47	2.04		760	0.58	MS-SPS	[46]
$Mg_{1.97}Li_{0.03}Ge_{0.4}Sn_{0.6}$	Li	1.26	595.95	167.24	16.57	2.25		700	0.52	BM-SPS	[47]
$Mg_{1.98}Li_{0.02}Si_{0.4}Sn_{0.6}$	Li	0.84	310.44	204.90	13.06	1.61		700	0.57	BM-SPS	[47]
$Mg_{1.96}Li_{0.04}Sn_{0.75}Ge_{0.25}$	Li	1.65	808.60	150.48	18.23	2.59		723	0.52	BM-HP	[48]
$Mg_2Si_{0.3}Sn_{0.7}$ + 0.5% Li	Li	1.60	383.25	181.37	12.61		1.46	650	0.45	Melting-annealing	[49]
$Mg_{1.97}Na_{0.03}Sn_{0.75}Ge_{0.25}$	Na	0.59	334.82	181.12	11.04	1.79		723	0.45	BM-HP	[48]
$Mg_2Sn_{0.73}Ga_{0.02}Ge_{0.25}$	Ga	1.52	603.18	158.16	15.03	2.42		623	0.39	BM-HP	[48]
$Mg_{2.10}(Si_{0.3}Sn_{0.7})_{0.95}Ga_{0.05}$	Ga	2.09	386.10	165.96	10.63	1.95		650	0.35	SSR-SPS	[50]
$Ag_{0.01}Mg_{1.99}Si$	Ag		486.09	179.22	15.61	3.45		770	0.35	BM-microwaving-SPS	[51]
Ag 3 mol. %-doped Mg_2Sn	Ag	0.76	827.33	123.23	12.56	3.96		600	0.18	Melting-annealing-SPS	[52]

[a]*BM* ball milling, *SPS* spark plasma sintering, *PECS* pulsed electric current sintering, *MS* melt spinning, *HP* hot pressing, and *SSR* solid state reaction

Table 4 Thermoelectric properties and typical synthesis methods of *p*-type doped higher manganese silicide (HMS)

Material	Dopant	n_c (10^{21} cm^{-3})	σ (S cm^{-1})	S (μV K^{-1})	PF (μW cm^{-1} K^{-2})	κ_{tot} (W m^{-1} K^{-1})	κ_{lat} (W m^{-1} K^{-1})	T (K)	ZT	Synthesis method[a]	References
$MnSi_{1.73}$:$Al_{0.005}$	Al		251.98	227.80	13.33	2.60		823	0.41	SSR-HP	[54]
1.9 at.% Al-doped $MnSi_{1.75}$	Al		345.00	230.00	18.20	2.00	1.35	773	0.70	GPA-SPS	[55]
5 at.% Al-doped $MnSi_{1.73}$	Al		300.00	205.00	12.70	1.70	1.10	873	0.65	SPS	[56]
5 at.% Al-doped $MnSi_{1.73}$	Al	1.90	240.00	250.00	15.00	1.50	1.10	800	0.80	MS-SPS	[57]
$Mn(Al_{0.0035}Ge_{0.015}Si_{0.9715})_{1.8}$	Al, Ge	2.38	353.23	223.74	17.63	2.57	2.17	823	0.57	SSR-BM-SPS	[58]
$Mn_{0.95}Fe_{0.05}Si_{1.662}Al_{0.1}$	Al, Fe	1.40	171.00	239.41	9.72	2.74	2.41	815	0.29	MS-SPS	[59]
$Mn_{0.96}V_{0.02}Si_{1.74}$	V		708.70	181.11	23.30			800	0.59	AM-MG	[60]
$Mn_{0.98}Cr_{0.02}Si_{1.80}$	Cr	0.22	310.27	214.40	14.20	3.07	2.13	823	0.38	BM-SPS	[61]
$Mn_{0.96}Co_{0.04}Si_{1.74}$	Co	3.20	492.47	190.98	17.83	2.88	1.91	800	0.5	AM-MG	[62]
$MnSi_{1.77}Ge_{0.027}$	Ge	2.83	428.17	203.72	17.25	2.39	1.75	823	0.61	SSR-SPS	[63]
$Mn(Ge_{0.015}Si_{0.985})_{1.75}$	Ge	2.60	425.00	200.00	16.90	2.30	1.80	840	0.62	TE-PAS	[64]
$Mn_{34.6}W_{1.8}Si_{63.6}$	W		370.51	188.98	13.23	1.85		700	0.50	AM-LQ-SPS	[65]
$Re_{6.0}Mn_{30.4}Si_{63.6}$	Re		448.43	226.95	23.10	2.09	1.01	920	1.04	AM-MS-SPS	[9, 66]
$Re_{0.04}Mn_{0.96}Si_{1.8}$	Re	1.70	275.00	240.00	16.00	2.25	1.90	800	0.57	SSR-BM-SPS	[35]
$Mn_{0.99}Re_{0.01}Si_{1.75}Ge_{0.025}$	Re, Ge	2.50	510.03	230.21	27.03	2.33	1.50	850	1.00	Melting-BM-SPS-shock wave	[67]

[a]*GPA* gas phase atomization, *LQ* liquid quenching, *MG* melt grown, *TE* thermal explosion, and *PAS* plasma activated sintering

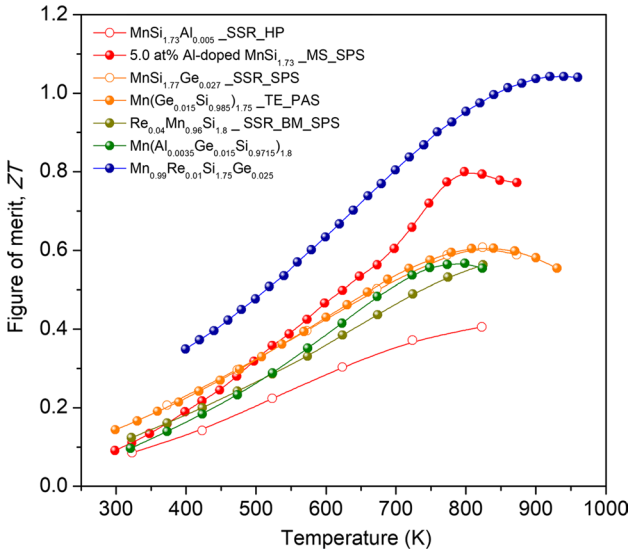

Fig. 4 Figure of merit, *ZT*, as function of temperature for *p*-type doped higher manganese silicide. Here, *SSR* solid state reaction, *MS* melt spinning, *TE* thermal explosion, *BM* ball milling, *HP* hot pressing, *SPS* spark plasma sintering, and *PAS* plasma activated sintering

nanowires and MnS were high (~0.7 and 0.6, respectively at 823 K). These values were achieved by reducing κ_{lat} to the theoretical limit [8, 34]. Additionally, the power factor of the HMS nanocomposites could be increased by controlling their band alignment. Precisely controlling the band gap and work function of the matrix and nanophases, led to the minimization of the decrease in μ_{Hall} at the interfaces; consequently, the power factor could be improved using the energy filtering and charge transfer effects. We fabricated metal NP-embedded HMS nanocomposites and HMS/metal silicide composites and determined that the increase in their power factors by the precise control of the band alignment and interfacial properties of these materials. Moreover, unexpected nanostructures (dislocations, precipitates, and secondary phases), induced by novel synthesis technique, led to the decrease in κ_{lat}, which, consequently, increased the *ZT* value [9, 55, 57, 66, 67, 84]. Nanostructure engineering, including the introduction of nanophases or heterostructures in HMS TE materials, is an effective route for increasing their power factors by controlling their interfacial properties, and also for decreasing κ_{lat} owing to the intensified phonon scattering at interfaces. Therefore, material design optimization should be implemented to maximize the increase in *ZT*.

2.3 Band Structure Modification

Band structure modification via the formation of point defects is an effective for increasing the power factor. Band structure modification strategies, including band convergence, band flattening, and resonant states, can increase the density of states near the Fermi level, which would result in the increase in *S* [86]. For Mg_2S-based compounds, pseudo-binary (Mg_2Si–Mg_2Sn, Mg_2Sn–Mg_2Ge, and Mg_2Sn–Mg_2Pb) and pseudo-ternary (Mg_2Si–Mg_2Sn–Mg_2Ge, Mg_2Si–Mg_2Sn–Mg_2Pb, and Mg_2Sn–Mg_2Ge–Mg_2Pb) systems contributed to the band convergence effect [5, 6, 24, 87–99]. Moreover, alloying Mg_2Si with Mg_2Sn, Mg_2Ge, or Mg_2Pb reduced the κ_{lat} values of these Mg_2Si-based compounds owing to the intensified phonon scattering by point defects and nanoparticles. Therefore, the convergence of the conduction bands could lead to high *ZT* values. Figure 8 and Table 7 show the *ZT* values of the above-mentioned doped pseudo-binary and pseudo-ternary systems [5, 6, 24, 87–102]. The *ZT* values of these systems were higher (> 1.0) than those of doped Mg_2Si (Fig. 2).

The TE quality factor, *B*, was introduced to elucidate the mechanism of the increase in *ZT* via band convergence. The *B* factor, which depends on the thermal and electronic transport properties of materials, and also on *ZT*, can be expressed as follows [86]:

$$B = \frac{2k_B h}{3\pi}\frac{N_v C_l}{m_I^* \Xi^2 \kappa_{lat}} T, \tag{6}$$

where *h* is the reduced Planck constant, N_v is the number of degenerated valleys of the band, C_l is the average longitudinal elastic moduli, m_I^* is the inertial effective mass, and Ξ is the deformation potential coefficient. The increase in N_v owing to the small energy separation (ΔE) between the light and heavy conduction bands (Fig. 9) led to the increase in *B*, which indicated that *ZT* could also be increased.

The Sb or Bi doped $Mg_2Si_{1-x}Sn_x$ ($0.4 \le x \le 0.7$) has a high *ZT* (> 1.0) owing to the decrease in κ_{lat} and the increase in *S* [5, 6, 24, 87–95, 99]. Yin et al. determined that an increase in Ge content in pseudo-ternary Mg_2Si–Mg_2Sn–Mg_2Ge system caused the improved *ZT* owing to smaller ΔE and the intensified phonon scattering [95]. Liu et al. investigated the pseudo-binary Mg_2Sn–Mg_2Ge system [96, 97]. The *ZT* value of $Mg_2Sn_{0.73}Ge_{0.25}Sb_{0.02}$ was higher than those of Mg_2Sn systems owing to band convergence and Ge alloying. Moreover, they determined that Ge alloying caused the weighted mobility to increase, band gap to widen, and κ_{lat} to decrease [96].

According to Eq. (3), if m^* is high, *S* will also be high. Increasing m^* via doping could be caused by the increase in m_b^*. However, m_b^* is related to the μ_{Hall} as follows:

$$m^* = N_v^{2/3} m_b^*, \tag{7}$$

where m_b^* is the band effective mass of a single valley.

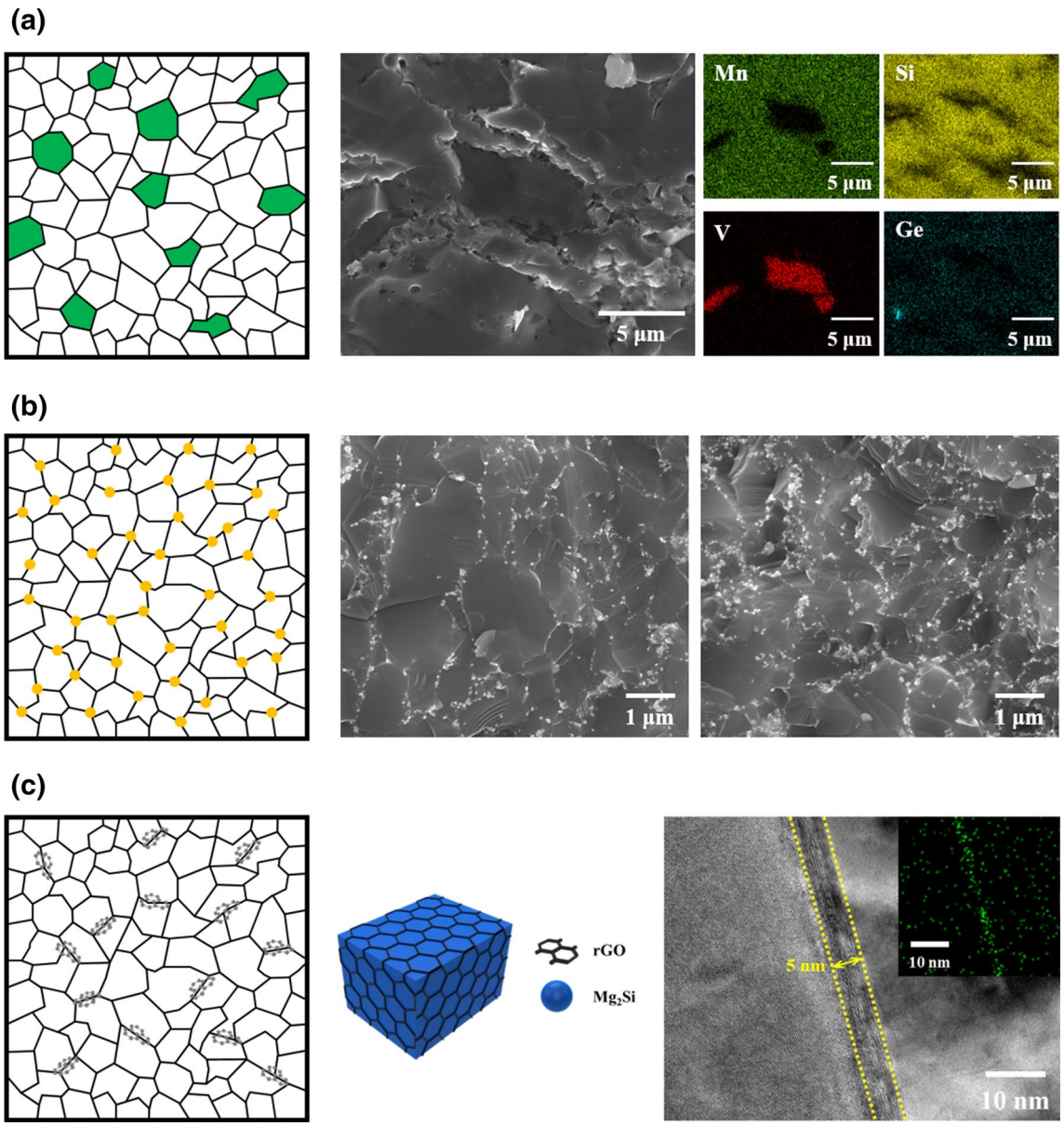

Fig. 5 Schematic, scanning electron microscopy, transmission electron microscopy, and energy-dispersive X-ray spectroscopy images of microstructure of silicide-based thermoelectric nanocomposites: **a** heterostructure, **b** nanoparticles/nanoinclusions, and **c** nanosheets/nanowires. Here, *rGO* reduced graphene oxide. Reprinted with permission from [1]. Copyright 2019 J. Korean Ceram. Soc.)

$$\mu_{Hall} \propto \frac{1}{m_b^{*5/2}}. \tag{8}$$

Therefore, increasing m^* via doping would not cause the power factor to increase owing to the decrease in σ, which was, in turn, caused by the decrease in μ_{Hall} [103]. Kim et al. [4] and Lee et al. [63] increased m^* by doping Mg_2Si and controlling the Si contents in HMS, and consequently, the power factor increased owing to the synergistic effect of the increase in n_c and m^* (Fig. 10a, b). Moreover, Gao et al. [67] and Shi et al. [104] increased the S value and power factor of HMS by tuning m^* using a new fabrication process: the rapid solidification and shock wave process.

Band structure modifications require precisely controlled doping strategies to achieve high TE properties. Therefore, it is important to systematically control the composition of TE materials, because precisely manipulating their band structure could lead to the increase in their TE properties.

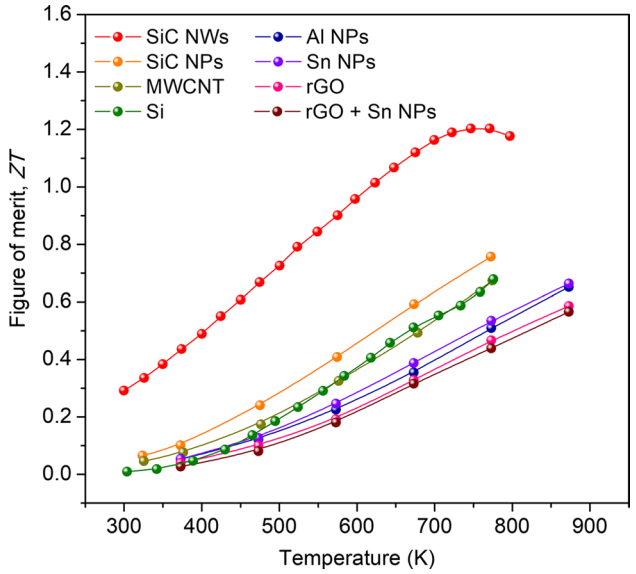

Fig. 6 Figure of merit, *ZT*, as function of temperature for *n*-type Mg_2Si nanocomposites. Here, *NWs* nanowires, *NPs* nanoparticles, *MWCNT* multi-wall carbon nanotube, and *rGO* reduced graphene oxide

3 Improving Mechanical Properties of Silicide Bulk Materials

Evaluating the chemical and thermal stability, and also the mechanical reliability of TE materials is essential for the fabrication and commercialization of TE modules. The mechanical reliability of TE materials is the most important factor because thermal stress, which is induced by the temperature differences between the hot and cold sides, could cause the fracture of TE materials, and consequently the breakdown of all electric circuits of TE modules. Moreover, ATEG systems should be reliable and should be able to withstand the vibrations and shocks that occur during vehicle operation. However, Mg_2Si-based compounds can be easily fractured owing to their inherent brittle fracture characteristics compared with those of other TE materials. Therefore, improving the mechanical reliability of Mg_2Si-based compounds should be pursued before fabricating silicide-based TE modules.

Fracture toughness (K_{Ic}) is an important factor for evaluating the mechanical reliability of materials. Materials that present high K_{Ic} exhibit high mechanical reliability because crack propagation does not occur actively when cracks form. Therefore, the introduction of secondary phases into materials is an effective strategy for enhancing their K_{Ic} by preventing the crack propagation.

Three representative mechanisms: crack propagation deflection, crack bridging, and sheet pull-out, could be used to increase K_{Ic} [105]. When cracks propagate, propagation is interrupted when a secondary phase that presents high

Table 5 Thermoelectric properties and typical synthesis methods of *n*-type Mg_2Si nanocomposites

Material	Nanophase	n_c (10^{20} cm^{-3})	σ (S cm^{-1})	S (μV K^{-1})	PF (μW cm^{-1} K^{-2})	κ_{tot} (W m^{-1} K^{-1})	κ_{lat} (W m^{-1} K^{-1})	T (K)	ZT	Synthesis method[a]	References
$Mg_{2.16}(Si_{0.3}Sn_{0.7})_{0.98}Sb_{0.02}$ + 0.008 SiC_W	SiC nanowires	2.35	1152.56	− 198.82	45.55	2.85		750	1.20	SSR-SPS	[72]
Al-doped Mg_2Si + 0.1% CaO	CaO		372.99	− 224.22	18.75	2.08	1.26	873	0.76	SSR-BM-SPS	[73]
Al and Bi co-doped Mg_2Si + NPs	Al	0.90	623.22	− 182.71	20.80	2.79	1.41	873	0.65	SSR-metal NPs decoration-SPS	[27]
Al and Bi co-doped Mg_2Si + NPs	Sn	0.95	575.43	− 190.44	20.87	2.61	1.35	873	0.70	SSR-metal NPs decoration-SPS	[27]
Al and Bi co-doped Mg_2Si + NPs	Cu	0.96	488.18	− 193.14	18.21	2.63	1.57	873	0.61	SSR-metal NPs decoration-SPS	[27]
Sb-doped Mg_2Si + Cu binder	Cu							873	0.81	PAS	[74]
$Mg_2Si_{0.676}Ge_{0.3}Bi_{0.024}$/0.5 wt% SiC	SiC	0.67	396.00	− 212.00	17.80	1.82	1.31	773	0.75	SSR-mixer mill-HP	[75]
$Mg_2Si_{0.877}Ge_{0.1}Bi_{0.023}$/0.5 wt% MWCNT	MWCNT	0.76	470.00	− 200.00	18.80	2.20	1.60	773	0.67	SSR-annealing-mixer mill-HP	[76]
Al and Bi co doped Mg_2Si + Sn NPs	Sn	0.97	529.28	− 190.58	19.22	2.53	1.61	873	0.66	SSR-metal NPs decoration-SPS	[77]
Al and Bi co doped Mg_2Si + rGO	rGO	0.59	375.27	− 195.57	14.35	2.14	1.34	873	0.59	SSR-wet chemical mixing-SPS	[68]
Al and Bi co doped Mg_2Si + rGO + Sn NPs	rGO + Sn	0.71	346.58	− 198.08	13.60	2.10	1.46	873	0.57	SSR-wet chemical mixing-metal NPs decoration-SPS	[78]
1 mol% Bi doped Mg_2Si + 2.5 mol% Si	Si	1.17	658.00	− 204.00	27.38	3.10	2.00	775	0.68	BM-SSR-SPS	[79]

[a]*NPs* nanoparticles

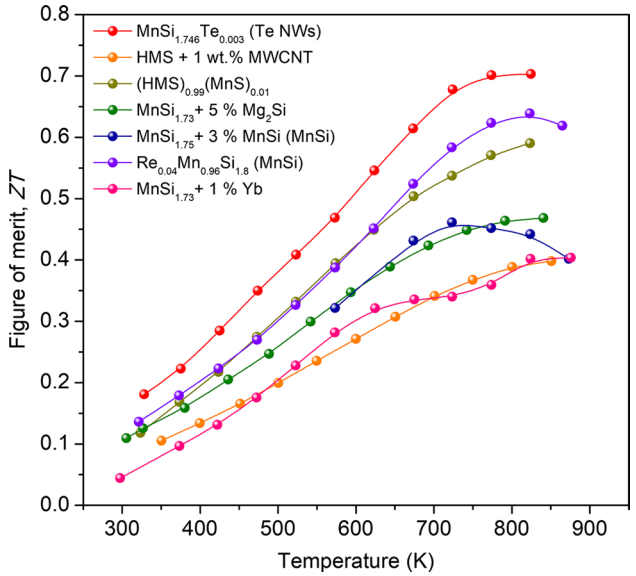

Fig. 7 Figure of merit, *ZT*, as function of temperature for *p*-type higher manganese silicide nanocomposites. Here, *NWs* nanowires and *MWCNT* multi-wall carbon nanotube

K_{Ic} is reached. This is the main mechanism for increasing K_{Ic} and can be observed when nanophases are introduced in nanocomposites [27, 77]. Crack bridging and pull-out are mechanisms for increasing K_{Ic} that occur mainly in nanocomposites with one-dimensional (1D) and two-dimensional (2D) nanophases. Low-dimensional nanophases can interfere with crack propagation by absorbing the crack propagation energy [68, 72]. Additionally, since the contact area of the 2D nanophase is wider than that of the 1D nanophase, crack propagation energy can be absorbed more effectively in nanocomposites with 2D nanophases [105]. Therefore, the contents, morphologies, and intrinsic properties of the nanophases should be precisely controlled, because K_{Ic} highly depends on the microstructure of nancomposites.

Kim et al. demonstrated the relationship between the TE properties and K_{Ic} values when various nanophases, such as metal NPs, rGO, and dual nanoinclusions, were introduced into Mg_2Si. They also reported the dependence of the TE and mechanical properties on the dimensions of the nanophases [27, 68, 77, 78]. Figure 11 shows the K_{Ic} values of Mg_2Si nanocomposites. The K_{Ic} of the 3-dimensional nanophases (metal NPs) was 1.10 MPa $m^{1/2}$ and was achieved via crack propagation deflection; nonetheless, the effect was insufficient owing to interface density saturation. However, for 2D nanophases, all three K_{Ic} enhancement mechanisms were activated, and the highest achieved K_{Ic} was 1.88 MPa $m^{1/2}$ [68]. Moreover, the crack propagation deflection mechanism was strengthened by introducing dual nanoinclusions (metal NPs and rGO), which resulted

Table 6 Thermoelectric properties and typical synthesis method of the *p*-type HMS nanocomposites

Material	Nanophase[a]	n_c (10^{20} cm^{-3})	σ (S cm^{-1})	S (μV K^{-1})	PF (μW cm^{-1} K^{-2})	κ_{tot} (W m^{-1} K^{-1})	κ_{lat} (W m^{-1} K^{-1})	T (K)	ZT	Synthesis method	References
$MnSi_{1.746}Te_{0.003}$	Te nanowire	2.00	300.00	230.00	15.90	1.86	1.50	823	0.70	Wet BM-SPS	[8]
HMS + 1 wt% MWCNT	MWCNT	3.00	271.17	211.94	12.23	2.62		850	0.40	BM-SPS	[81]
$(HMS)_{0.99}(MnS)_{0.01}$	MnS	1.87	295.97	224.67	14.94	2.09	1.49	823	0.59	BM-SPS	[34]
$MnSi_{1.73}$ + 5% Mg_2Si	Mg_2Si	1.21	326.68	222.56	16.15	2.69	2.39	773	0.47	Melting-BM-SPS	[82]
$MnSi_{1.75}$ + 3% MnSi	In situ nanoscale MnSi	0.29	408.53	206.55	17.28	2.75	2.03	723	0.46	IM-quenching-SPS	[83]
$Re_{0.04}Mn_{0.96}Si_{1.8}$	In situ nanoscale MnSi	2.30	375.81	227.92	19.11	2.49	2.00	823	0.64	Melting-quenching-BM-SPS	[84]
$MnSi_{1.73}$ + 1% Yb	Yb	1.75	384.62	191.73	14.14	3.06		873	0.40	Wet BM-SPS	[85]

[a]*MWCNT* multi-walled carbon nanotube

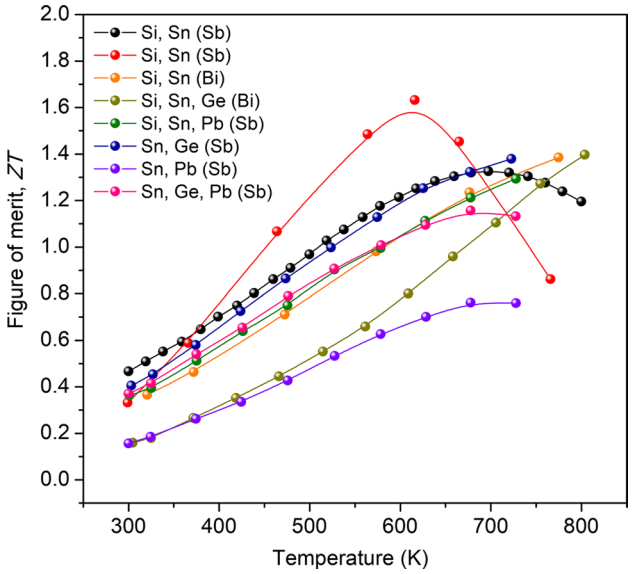

Fig. 8 Figure of merit, *ZT*, as function of temperature for *n*-type pseudo-binary (Mg_2Si–Mg_2Sn, Mg_2Sn–Mg_2Ge, and Mg_2Sn–Mg_2Pb) and pseudo-ternary (Mg_2Si–Mg_2Sn–Mg_2Ge, Mg_2Si–Mg_2Sn–Mg_2Pb, and Mg_2Sn–Mg_2Ge–Mg_2Pb) systems

in the high K_{Ic} value of 2.26 MPa $m^{1/2}$ [78]. Additionally, Yin et al. achieved the K_{Ic} value of 1.36 MPa $m^{1/2}$ by introducing SiC nanowires at the grain boundaries and studied the effect of the nanophase morphology (nanoparticles and nanowires) on the mechanical reliability behavior of materials [72].

However, a significant trade-off relationship exists between *ZT* and K_{Ic}. Figure 12 depicts the relationship between *ZT* and K_{Ic} for Mg_2Si nanocomposites. The increase in interface density between the nanophase and the matrix caused the decrease in TE properties of Mg_2Si nanocomposites due to the decrease in μ_{Hall}. Therefore, it is important to identify an optimal nanophase that could improve the mechanical properties of materials while maintaining their TE properties. Moreover, it is important to design rule that can achieve a high trade-off relationship between the TE and mechanical properties of TE materials.

4 Summary and Perspective

Herein, we summarize the methods for increasing the TE and mechanical properties of silicide-based TE materials. Although silicide-based TE materials have received significant attention as ATEGs, their practical applications are still hindered by many limitations. Various strategies, such as composition tuning, n_c optimization, nanostructuring, nanocomposite engineering, band convergence, and effective mass tuning, have been used to overcome these limitations, and led to achieving *ZT* values of 1.6 and 1.0 for *n*-type Mg_2Si and *p*-type HMS, respectively. Moreover, the high K_{Ic} value of 2.26 MPa $m^{1/2}$ was achieved for Mg_2Si via the introduction of nanophases to overcome its low mechanical reliability. However, researchers should continue to develop strategies for improving the TE properties and mechanical reliability of the silicide-bases TE materials. Band and nanostructure engineering were particularly important for overcoming the trade-off relationships between n_c and *S*, μ_{Hall} and κ_{lat}, and *ZT* and K_{Ic}. Moreover, the novel technique that enables us to design the material is a prerequisite. Hence, a systematic strategy that combines calculations and experimental results should be established to achieve the optimized composition and microstructure design.

Moreover, not only the development of TE materials but also the development of bonding, diffusion barrier, and electrode materials are required. Research on increasing the mechanical properties of TE materials, engineering surface coating and sealing technologies to improve the chemical stability of silicide-based materials, and developing diffusion barrier and bonding materials are important research areas for expanding the commercial applications of silicide-based TE modules.

Although researchers are still facing challenges in their attempts to improve the TE properties of silicide-based TE materials and to develop high-efficiency TE modules, systematic studies and efforts could lead to significant progress in this field.

Acknowledgements This work was supported by the National Research Foundation of Korea (NRF) Grant (2017R1A2A1A17069528) and Basic Science Research Program funded by the Korea Government (MSIT) and the Ministry of Education (NRF-2019R1A6A1A11055660).

References

1. G. Kim, W. Kim, W. Lee, J. Korean Ceram. Soc. **56**, 435–442 (2019)
2. S.I. Kim, K.H. Lee, H.A. Mun, H.S. Kim, S.W. Hwang, J.W. Roh, D.J. Yang, W.H. Shin, X.S. Li, Y.H. Lee, G.J. Snyder, S.W. Kim, Science **348**, 109–114 (2015)
3. W.-S. Liu, Q. Zhang, Y. Lan, S. Chen, X. Yan, Q. Zhang, H. Wang, D. Wang, G. Chen, Z. Ren, Adv. Energy Mater. **1**, 577–587 (2011)
4. G. Kim, J. Kim, H. Lee, S. Cho, I. Lyo, S. Noh, B.-W. Kim, S.W. Kim, K.H. Lee, W. Lee, Scr. Mater. **116**, 11–15 (2016)
5. W. Liu, X. Tan, K. Yin, H. Liu, X. Tang, J. Shi, Q. Zhang, C. Uher, Phys. Rev. Lett. **108**, 166601 (2012)

Table 7 Thermoelectric properties and typical synthetic method of the *n*-type pseudo-binary (Mg_2Si–Mg_2Sn, Mg_2Si–Mg_2Ge, Mg_2Sn–Mg_2Ge, and Mg_2Sn–Mg_2Pb) and pseudo-ternary (Mg_2Si–Mg_2Sn–Mg_2Ge, Mg_2Si–Mg_2Sn–Mg_2Pb, and Mg_2Sn–Mg_2Ge–Mg_2Pb) systems

Material	Dopant	Alloying elements	n_c (10^{20} cm^{-3})	σ (S cm^{-1})	S (μV K^{-1})	PF (μW cm^{-1} K^{-2})	κ_{tot} (W m^{-1} K^{-1})	κ_{lat} (W m^{-1} K^{-1})	T (K)	ZT	Synthesis method	References
$Mg_2Si_{0.677}Ge_{0.3}Bi_{0.023}$	Bi	Si. Ge	0.69	396.00	−200.00	15.84	1.71	1.22	773	0.71	SSR-annealing-HP	[100]
$La_{0.01}Mg_{1.99}Si_{0.49}Ge_{0.5}Sb_{0.01}$	Sb, La	Si, Ge	0.70	859.26	−185.06	29.74	2.20	0.55	823	1.00	SSR-annealing-SPS	[101]
$Al_{0.05}Mg_2Si_{0.73}Sn_{0.27}$	Al	Si, Sn	1.16	215.18	−269.26	15.67	1.96		790	0.63	SSR-SPS	[102]
$Mg_2Si_{0.5875}Sn_{0.4}Sb_{0.0125}$	Sb	Si, Sn	2.70	893.31	−211.55	39.93	2.19		783	1.40	GPA-SPS	[87]
Sb doped $Mg_2Si_{0.5}Sn_{0.5}$	Sb	Si, Sn		469.92	−234.89	25.81	0.98	0.49	615	1.63	Melting-SPS (press-less sintering)	[6]
$Mg_{2.2}Si_{0.49}Sn_{0.5}Sb_{0.01}$	Sb	Si, Sn	1.92	635.99	−226.58	32.65	2.08	1.15	800	1.25	SSR-SPS	[88]
$Mg_{2.16}Si_{0.45}Sn_{0.537}Sb_{0.013}$	Sb	Si, Sn	2.03	785.60	−207.82	33.93	2.48	1.55	725	1.00	Flux method-HP	[89]
$Mg_2(Si_{0.4}Sn_{0.6})Sb_{0.018}$	Sb	Si, Sn	1.82	724.62	−230.50	38.50	1.85	0.66	673	1.40	BM-SPS	[90]
$Mg_{2.16}(Si_{0.4}Sn_{0.6})_{0.985}Sb_{0.015}$	Sb	Si, Sn	1.67	736.53	−221.94	36.46	2.06	1.97	740	1.30	SSR-SPS	[91]
$Mg_2Si_{1-x}Sn_xSb$	Sb	Si, Sn	1.70	778.74	−235.72	44.32	2.33		700	1.30	SSR-SPS	[5]
$Mg_{2.08}Si_{0.37}Sn_{0.6}Bi_{0.03}$	Bi	Si, Sn		1021.28	−207.14	44.18	2.18		773	1.55	Flux method-PECS	[24]
$Mg_2Si_{0.3}Sn_{0.665}Bi_{0.035}$	Bi	Si, Sn	3.00	1024.31	−205.94	43.44	2.40	0.99	773	1.40	SSR-BM-HP	[92]
$Mg_2(Si_{0.3}Sn_{0.7})_{0.985}Bi_{0.015}$	Bi	Si, Sn	2.05	938.93	−214.50	43.09	2.39	1.32	700	1.30	SSR-SPS	[93]
$Mg_2Si_{0.5375}Sn_{0.4}Ge_{0.05}Sb_{0.0125}$	Sb	Si, Sn, Ge		667.93	−221.55	32.78	2.17	1.30	800	1.20	SSR-BM-annealing-HP	[94]
$Mg_{2.16}(Si_{0.3}Ge_{0.05}Sn_{0.65})_{0.98}Sb_{0.02}$	Sb	Si, Sn, Ge		967.32	−215.52	45.00	2.35	1.85	750	1.45	SSR-SPS	[95]
$Mg_2Si_{0.53}Sn_{0.4}Ge_{0.05}Bi_{0.02}$	Bi	Si, Sn, Ge		747.18	−215.51	34.70	1.98	1.04	800	1.40	SSR-BM-annealing-HP	[94]
$Mg_2Sn_{0.73}Ge_{0.25}Sb_{0.02}$	Sb	Sn, Ge		994.29	−227.64	51.79	2.79		723	1.40	BM-HP	[96]
$Mg_2Sn_{0.73}Ge_{0.25}Sb_{0.02}$	Sb	Sn, Ge		1112.72	−220.09	53.93	2.74	1.20	723	1.40	BM-HP	[97]
$Mg_2Sn_{0.73}Ge_{0.25}Bi_{0.02}$	Bi	Sn, Ge	1.63	1095.01	−217.84	51.54	2.50		673	1.40	BM-HP	[98]
$Mg_2Sn_{0.93}Pb_{0.05}Sb_{0.02}$	Sb	Sn, Pb		1679.69	−170.81	48.06	4.29	2.41	676	0.77	BM-HP	[99]
$Mg_2Sn_{0.63}Si_{0.3}Pb_{0.05}Sb_{0.02}$	Sb	Si, Sn, Pb	2.83	1102.21	−206.69	46.34	2.61	1.38	723	1.30	BM-HP	[99]
$Mg_2Sn_{0.68}Ge_{0.25}Pb_{0.05}Sb_{0.02}$	Sb	Sn, Ge, Pb	2.30	960.25	−212.11	43.59	2.55	1.52	673	1.20	BM-HP	[99]

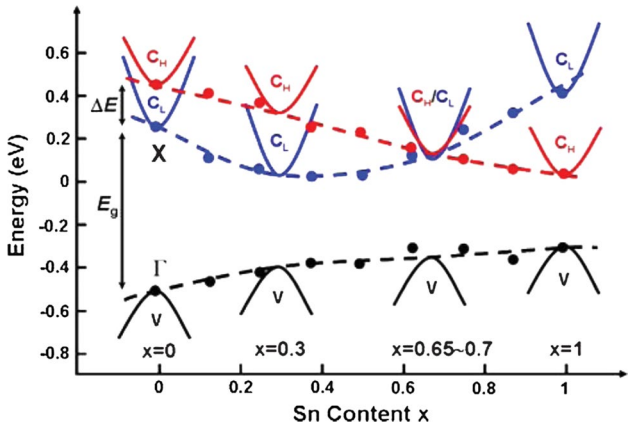

Fig. 9 Schematic electronic band structure of Mg_2Si–Mg_2Sn system as function of Sn content. Here, C_H = heavy conduction band, C_L = light conduction band, E_g = band gap, ΔE = energy separation between C_L and C_H, and V = valence band. Reprinted with permission from [5]. Copyright 2012 American Physical Society)

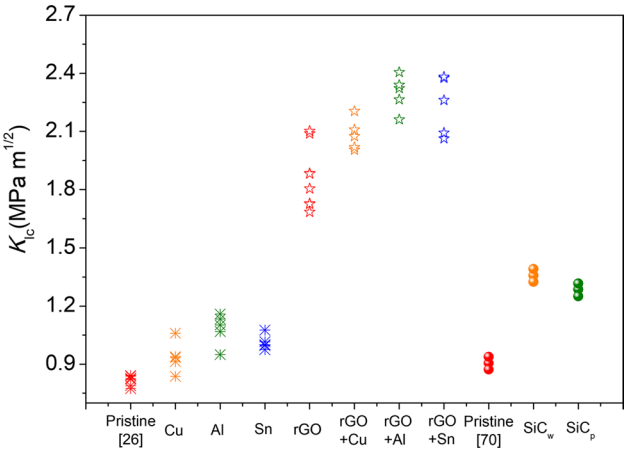

Fig. 11 Fracture toughness, K_{Ic}, values of various Mg_2Si nanocomposites. Here, *rGO* reduced graphene oxide, SiC_w SiC wire, and SiC_p SiC particle

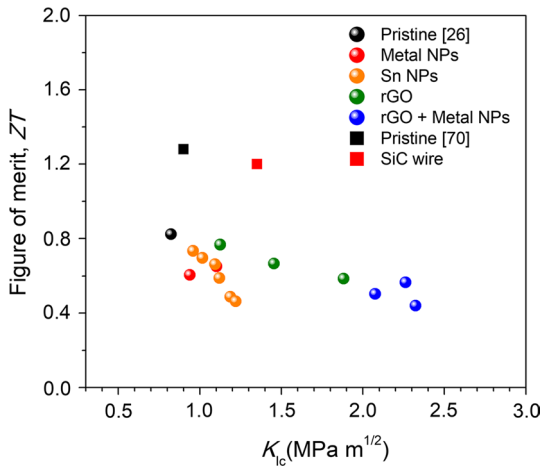

Fig. 12 Dependence of fracture toughness (K_{Ic}) on figure of merit, *ZT* for various Mg_2Si nanocomposites

6. H. Ning, G.D. Mastrorillo, S. Grasso, B. Du, T. Mori, C. Hu, Y. Xu, K. Simpson, G. Maizza, M.J. Reece, J. Mater. Chem. A **3**, 17426–17432 (2015)
7. P. Gao, J.D. Davis, V.V. Poltavets, T.P. Hogan, J. Mater. Chem. C **4**, 929–934 (2016)
8. Z. Li, J.-F. Dong, F.-H. Sun, S. Hirono, J.-F. Li, Chem. Mater. **29**, 7378–7389 (2017)
9. A. Yamamoto, S. Ghodke, H. Miyazaki, M. Inukai, Y. Nishino, M. Matsunami, T. Takeuchi, Jpn. J. Appl. Phys. **55**, 020301 (2016)
10. S. Chen, K.C. Lukas, W. Liu, C.P. Opeil, G. Chen, Z. Ren, Adv. Energy Mater. **3**, 1210–1214 (2013)
11. W. Zhao, Z. Liu, Z. Sun, Q. Zhang, P. Wei, X. Mu, H. Zhou, C. Li, S. Ma, D. He, P. Ji, W. Zhu, X. Nie, X. Su, X. Tang, B. Shen, X. Dong, J. Yang, Y. Liu, J. Shi, Nature **549**, 247–251 (2017)
12. G. Rogl, A. Grytsiv, P. Rogl, N. Peranio, E. Bauer, M. Zehetbauer, O. Eibl, Acta Mater. **63**, 30–43 (2014)
13. M.S. Kim, W.J. Lee, K.H. Cho, J.P. Ahn, Y.M. Sung, ACS Nano **10**, 7197–7207 (2016)

Fig. 10 Seebeck coefficient, *S*, as function of carrier concentration, n_c, of **a** *n*-type Mg_2Si at 873 K and **b** *p*-type higher manganese silicide at 300 K [4, 63]

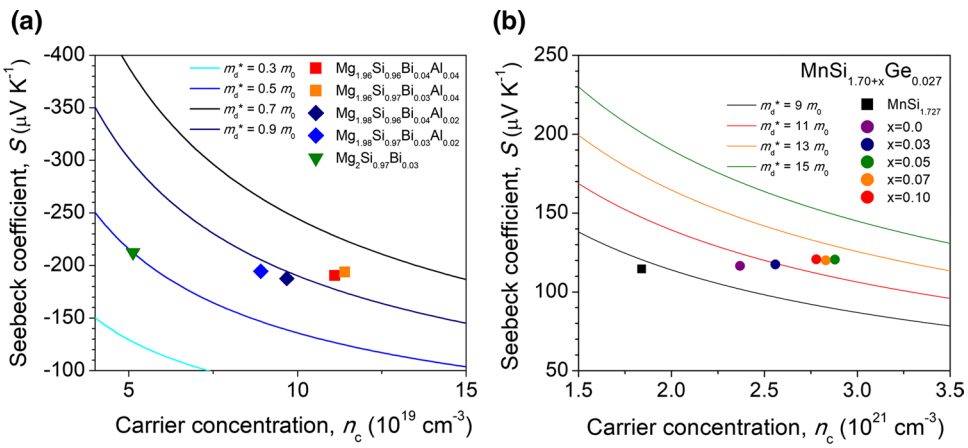

14. Y. Pei, G. Tan, D. Feng, L. Zheng, Q. Tan, X. Xie, S. Gong, Y. Chen, J.-F. Li, J. He, M.G. Kanatzidis, L.-D. Zhao, Adv. Energy Mater. **7**, 1601450 (2017)
15. K. Biswas, J. He, Q. Zhang, G. Wang, C. Uher, V.P. Dravid, M.G. Kanatzidis, Nat. Chem. **3**, 160–166 (2011)
16. K. Biswas, J. He, I.D. Blum, C.I. Wu, T.P. Hogan, D.N. Seidman, V.P. Dravid, M.G. Kanatzidis, Nature **489**, 414–418 (2012)
17. L.D. Zhao, S. Hao, S.H. Lo, C.I. Wu, X. Zhou, Y. Lee, H. Li, K. Biswas, T.P. Hogan, C. Uher, C. Wolverton, V.P. Dravid, M.G. Kanatzidis, J. Am. Chem. Soc. **135**, 7364–7370 (2013)
18. R. Nunna, P. Qiu, M. Yin, H. Chen, R. Hanus, Q. Song, T. Zhang, M.-Y. Chou, M.T. Agne, J. He, G.J. Snyder, X. Shi, L. Chen, Energy Environ. Sci. **10**, 1928–1935 (2017)
19. E.S. Toberer, C.A. Cox, S.R. Brown, T. Ikeda, A.F. May, S.M. Kauzlarich, G.J. Snyder, Adv. Funct. Mater. **18**, 2795–2800 (2008)
20. Z.-Y. Li, J.-F. Li, Adv. Energy Mater. **4**, 1300937 (2014)
21. C. Chang, M. Wu, D. He, Y. Pei, C.-F. Wu, X. Wu, H. Yu, F. Zhu, K. Wang, Y. Chen, L. Huang, J.-F. Li, J. He, L.-D. Zhao, Science **360**, 778–783 (2018)
22. L.D. Zhao, S.H. Lo, Y. Zhang, H. Sun, G. Tan, C. Uher, C. Wolverton, V.P. Dravid, M.G. Kanatzidis, Nature **508**, 373–377 (2014)
23. W.-J. Jung, I.-H. Kim, Met. Mater. Int. **24**, 415–421 (2018)
24. P. Gao, X. Lu, I. Berkun, R.D. Schmidt, E.D. Case, T.P. Hogan, Appl. Phys. Lett. **105**, 202104 (2014)
25. D. Kato, K. Iwasaki, M. Yoshino, T. Yamada, T. Nagasaki, J. Solid State Chem. **258**, 93–98 (2018)
26. J. de Boor, T. Dasgupta, H. Kolb, C. Compere, K. Kelm, E. Mueller, Acta Mater. **77**, 68–75 (2014)
27. G. Kim, H. Lee, J. Kim, J.W. Roh, I. Lyo, B.W. Kim, K.H. Lee, W. Lee, Ceram. Int. **43**, 12979–12982 (2017)
28. A.L.S. Jeremy, M. Higgins, I.A. Guzei, S. Jin, J. Am. Chem. Soc. **130**, 16086–16094 (2008)
29. W.-D. Liu, Z.-G. Chen, J. Zou, Adv. Energy Mater. **8**, 1800056 (2018)
30. H.W. Knott, M.H. Mueller, L. Heaton, Acta Crystallogr. **23**, 549–555 (1967)
31. Y. Miyazaki, D. Igarashi, K. Hayashi, T. Kajitani, K. Yubuta, Phys. Rev. B **78**, 214104 (2008)
32. M.S.I. Kawasumi, I. Nishida, K. Masumoto, J. Mater. Sci. **16**, 355–366 (1981)
33. G. Kim, H.J. Rim, K.H. Lee, J.W. Roh, W. Lee, Ceram. Int. **45**, 19538–19541 (2019)
34. Z. Li, J.F. Dong, F.H. Sun, Asfandiyar, Y. Pan, S.F. Wang, Q. Wang, D. Zhang, L. Zhao, J.F. Li, Adv. Sci. **5**, 1800626 (2018)
35. X. Chen, S.N. Girard, F. Meng, E. Lara-Curzio, S. Jin, J.B. Goodenough, J. Zhou, L. Shi, Adv. Energy Mater. **4**, 1400452 (2014)
36. J.I. Tani, H. Kido, Phys. B **364**, 218–224 (2005)
37. J.-I. Tani, H. Kido, Intermetallics **15**, 1202–1207 (2007)
38. S.K. Bux, M.T. Yeung, E.S. Toberer, G.J. Snyder, R.B. Kaner, J.-P. Fleurial, J. Mater. Chem. **21**, 12259–12266 (2011)
39. S. Battiston, S. Fiameni, M. Saleemi, S. Boldrini, A. Famengo, F. Agresti, M. Stingaciu, M.S. Toprak, M. Fabrizio, S. Barison, J. Electron. Mater. **42**, 1956–1959 (2013)
40. J.E. Lee, S.H. Cho, M.W. Oh, B. Ryu, S.J. Joo, B.S. Kim, B.K. Min, H.W. Lee, S.D. Park, Electron. Mater. Lett. **10**, 807–811 (2014)
41. S. Muthiah, B. Sivaiah, B. Gahtori, K. Tyagi, A.K. Srivastava, B.D. Pathak, A. Dhar, R.C. Budhani, J. Electron. Mater. **43**, 2035–2039 (2014)
42. K. Mitra, G.K. Goyal, E. Rathore, K. Biswas, S. Vitta, S. Mahapatra, T. Dasgupta, Phys. Status Solidi A **215**, 1700829 (2018)
43. S. Muthiah, J. Pulikkotil, A.K. Srivastava, A. Kumar, B.D. Pathak, A. Dhar, R.C. Budhani, Appl. Phys. Lett. **103**, 053901 (2013)
44. Q.S. Meng, W.H. Fan, R.X. Chen, Z.A. Munir, J. Alloys Compd. **509**, 7922–7926 (2011)
45. H. Kamila, P. Sahu, A. Sankhla, M. Yasseri, H.-N. Pham, T. Dasgupta, E. Mueller, J. de Boor, J. Mater. Chem. A **7**, 1045–1054 (2019)
46. X. Tang, G. Wang, Y. Zheng, Y. Zhang, K. Peng, L. Guo, S. Wang, M. Zeng, J. Dai, G. Wang, X. Zhou, Scr. Mater. **115**, 52–56 (2016)
47. J. de Boor, U. Saparamadu, J. Mao, K. Dahal, E. Müller, Z. Ren, Acta Mater. **120**, 273–280 (2016)
48. U. Saparamadu, J. de Boor, J. Mao, S. Song, F. Tian, W. Liu, Q. Zhang, Z. Ren, Acta Mater. **141**, 154–162 (2017)
49. G.N. Isachenko, A.Y. Samunin, E.A. Gurieva, M.I. Fedorov, D.A. Pshenay-Severin, P.P. Konstantinov, M.D. Kamolova, J. Electron. Mater. **45**, 1982 (2016)
50. W. Liu, K. Yin, X. Su, H. Li, Y. Yan, X. Tang, C. Uher, Intermetallics **32**, 352–361 (2013)
51. D. Berthebaud, F. Gascoin, J. Solid State Chem. **202**, 61–64 (2013)
52. S.M. Choi, T.H. An, W.S. Seo, C. Park, I.H. Kim, S.U. Kim, J. Electron. Mater. **41**, 1071–1076 (2012)
53. D.B. Migas, V.L. Shaposhnikov, A.B. Filonov, V.E. Borisenko, N.N. Dorozhkin, Phys. Rev. B **77**, 075205 (2008)
54. D.K. Shin, S.W. You, I.H. Kim, J. Korean Phys. Soc. **64**, 1412–1415 (2014)
55. G. Bernard-Granger, M. Soulier, H. Ihou-Mouko, C. Navone, M. Boidot, J. Leforestier, J. Simon, J. Alloys Compd. **618**, 403–412 (2015)
56. S. Muthiah, R.C. Singh, B.D. Pathak, A. Dhar, Scr. Mater. **119**, 60–64 (2016)
57. S. Muthiah, R.C. Singh, B.D. Pathak, P.K. Avasthi, R. Kumar, A. Kumar, A.K. Srivastava, A. Dhar, Nanoscale **10**, 1970–1977 (2018)
58. X. Chen, A. Weathers, D. Salta, L. Zhang, J. Zhou, J.B. Goodenough, L. Shi, J. Appl. Phys. **114**, 173705 (2013)
59. S.A. Barczak, R.A. Downie, S.R. Popuri, R. Decourt, M. Pollet, J.W.G. Bos, J. Solid State Chem. **227**, 55–59 (2015)
60. Y. Miyazaki, H. Hamada, K. Hayashi, K. Yubuta, J. Electron. Mater. **46**, 2705–2709 (2016)
61. G. Liu, Q. Lu, X. Zhang, J. Zhang, Y. Shi, J. Electron. Mater. **41**, 1450–1455 (2011)
62. H. Nagai, H. Hamada, K. Hayashi, Y. Miyazaki, J. Electron. Mater. **48**, 1902–1908 (2019)
63. H. Lee, G. Kim, B. Lee, J. Kim, S.-M. Choi, K.H. Lee, W. Lee, Scr. Mater. **135**, 72–75 (2017)
64. X. She, X. Su, H. Du, T. Liang, G. Zheng, Y. Yan, R. Akram, C. Uher, X. Tang, J. Mater. Chem. C **3**, 12116–12122 (2015)
65. S. Ghodke, N. Hiroishi, A. Yamamoto, H. Ikuta, M. Matsunami, T. Takeuchi, J. Electron. Mater. **45**, 5279–5284 (2016)
66. T.K.T. Homma, N. Saito, S. Ghodke, T. Takeuchi, J. Alloys Compd. **776**, 8–15 (2019)
67. Z. Gao, Z. Xiong, J. Li, C. Lu, G. Zhang, T. Zeng, Y. Ma, G. Ma, R. Zhang, K. Chen, T. Zhang, Y. Liu, J. Yang, L. Cao, K. Jin, J. Mater. Chem. A **7**, 3384–3390 (2019)
68. G. Kim, S.W. Kim, H.J. Rim, H. Lee, J. Kim, J.W. Roh, B.-W. Kim, K.H. Lee, W. Lee, Scr. Mater. **162**, 402–407 (2019)
69. N. Satyala, D. Vashaee, Appl. Phys. Lett. **100**, 073107 (2012)
70. N. Satyala, D. Vashaee, J. Appl. Phys. **112**, 093716 (2012)
71. P. Norouzzadeh, Z. Zamanipour, J.S. Krasinski, D. Vashaee, J. Appl. Phys. **112**, 124308 (2012)
72. K. Yin, X. Su, Y. Yan, H. Tang, M.G. Kanatzidis, C. Uher, X. Tang, Scr. Mater. **126**, 1–5 (2017)
73. T. Itoh, A. Tominaga, Mater. Trans. **57**, 1088–1093 (2016)

74. M. Ishikawa, T. Nakamura, S. Hirata, T. Iida, K. Nishio, Y. Kogo, Jpn. J. Appl. Phys. **54**, 07JC03 (2015)
75. N. Farahi, S. Prabhudev, M. Bugnet, G.A. Botton, J.R. Salvador, H. Kleinke, J. Electron. Mater. **45**, 6052–6058 (2016)
76. N. Farahi, S. Prabhudev, M. Bugnet, G.A. Botton, J. Zhao, J.S. Tse, J.R. Salvador, H. Kleinke, RSC Adv. **5**, 65328–65336 (2015)
77. G. Kim, H. Lee, H.J. Rim, J. Kim, K. Kim, J.W. Roh, S.-M. Choi, B.-W. Kim, K.H. Lee, W. Lee, J. Alloys Compd. **769**, 53–58 (2018)
78. G. Kim, H.J. Rim, H. Lee, J. Kim, J.W. Roh, K.H. Lee, W. Lee, J. Alloys Compd. **801**, 234–238 (2019)
79. T. Yi, S. Chen, S. Li, H. Yang, S. Bux, Z. Bian, N.A. Katcho, A. Shakouri, N. Mingo, J.P. Fleurial, N.D. Browning, S.M. Kauzlarich, J. Mater. Chem. **22**, 24805–24813 (2012)
80. B. Zhang, T. Zheng, Q. Wang, Y. Zhu, H.N. Alshareef, M.J. Kim, B.E. Gnade, J. Alloys Compd. **699**, 1134–1139 (2017)
81. D.Y.N. Truong, H. Kleinke, F. Gascoin, Dalton Trans. **43**, 15092–15097 (2014)
82. W.-D. Liu, X.-L. Shi, R. Moshwan, Q. Sun, L. Yang, Z.-G. Chen, J. Zou, J. Mater. Chem. C **7**, 7212–7218 (2019)
83. R. Zhao, F. Guo, Y. Shu, X. Zhang, Q. Lu, J. Zhang, JOM **66**, 2298–2308 (2014)
84. X. Chen, J. Zhou, J.B. Goodenough, L. Shi, J. Mater. Chem. C **3**, 10500–10508 (2015)
85. M. Saleemi, A. Famengo, S. Fiameni, S. Boldrini, S. Battiston, M. Johnsson, M. Muhammed, M.S. Toprak, J. Alloys Compd. **619**, 31–37 (2015)
86. Y. Pei, H. Wang, G.J. Snyder, Adv. Mater. **24**, 6125–6135 (2012)
87. G. Bernard-Granger, C. Navone, J. Leforestier, M. Boidot, K. Romanjek, J. Carrete, J. Simon, Acta Mater. **96**, 437–451 (2015)
88. W. Liu, X. Tang, H. Li, J. Sharp, X. Zhou, C. Uher, Chem. Mater. **23**, 5256–5263 (2011)
89. X. Liu, T. Zhu, H. Wang, L. Hu, H. Xie, G. Jiang, G.J. Snyder, X. Zhao, Adv. Energy Mater. **3**, 1238–1244 (2013)
90. L. Zheng, X. Zhang, H. Liu, S. Li, Z. Zhou, Q. Lu, J. Zhang, F. Zhang, J. Alloys Compd. **671**, 452–457 (2016)
91. W. Liu, X. Tang, H. Li, K. Yin, J. Sharp, X. Zhou, C. Uher, J. Mater. Chem. **22**, 13653–13661 (2012)
92. N. Farahi, S. Prabhudev, G.A. Botton, J.R. Salvador, H. Kleinke, ACS Appl. Mater. Interfaces **8**, 34431–34437 (2016)
93. W. Liu, H. Chi, H. Sun, Q. Zhang, K. Yin, X. Tang, Q. Zhang, C. Uher, Phys. Chem. Chem. Phys. **16**, 6893–6897 (2014)
94. A.U. Khan, N. Vlachos, T. Kyratsi, Scr. Mater. **69**, 606–609 (2013)
95. K. Yin, X. Su, Y. Yan, Y. You, Q. Zhang, C. Uher, M.G. Kanatzidis, X. Tang, Chem. Mater. **28**, 5538–5548 (2016)
96. W. Liu, J. Zhou, Q. Jie, Y. Li, H.S. Kim, J. Bao, G. Chen, Z. Ren, Energy Environ. Sci. **9**, 530–539 (2016)
97. W. Liu, H.S. Kim, S. Chen, Q. Jie, B. Lv, M. Yao, Z. Ren, C.P. Opeil, S. Wilson, C.W. Chu, Z. Ren, Proc. Natl. Acad. Sci. U. S. A. **112**, 3269–3274 (2015)
98. U. Saparamadu, J. Mao, K. Dahal, H. Zhang, F. Tian, S. Song, W. Liu, Z. Ren, Acta Mater. **124**, 528–535 (2017)
99. J. Mao, Y. Wang, B. Ge, Q. Jie, Z. Liu, U. Saparamadu, W. Liu, Z. Ren, Phys. Chem. Chem. Phys. **18**, 20726–20737 (2016)
100. N. Farahi, S. Prabhudev, G.A. Botton, J. Zhao, J.S. Tse, Z. Liu, J.R. Salvador, H. Kleinke, J. Alloys Compd. **644**, 249–255 (2015)
101. X. Zhou, G. Wang, H. Chi, X. Su, J.R. Salvador, W. Liu, X. Tang, C. Uher, J. Electron. Mater. **41**, 1589–1594 (2012)
102. X. Hu, M.R. Barnett, A. Yamamoto, J. Alloys Compd. **649**, 1060–1065 (2015)
103. Y. Pei, Z.M. Gibbs, A. Gloskovskii, B. Balke, W.G. Zeier, G.J. Snyder, Adv. Energy Mater. **4**, 1400486 (2014)
104. X. Shi, X. Shi, Y. Li, Y. He, L. Chen, Q. Li, J. Appl. Phys. **116**, 245104 (2014)
105. L.S. Walker, V.R. Marotto, M.A. Rafiee, N. Koratkar, E.L. Corral, ACS Nano **5**, 3182–3190 (2011)